

Short Communication

Transition from Pits to Stress Corrosion Cracking of SAE 4120 Steel in Simulated Oilfield Environment

Bingying Wang^{1,*}, Yige Liu¹, Zhiwei Gao¹, Tongle Zhang¹, Feng Yang², Shouqin Li²

¹School of Materials Science and Engineering, China University of Petroleum (East China), Qingdao 266580, China

²Dongxin Oil Production Plant, Shengli Oilfield Company, SINOPEC, Dongying 257094, China

*E-mail: tdwby2004@126.com

Received: 30 June 2020 / Accepted: 26 October 2020 / Published: 31 December 2020

SAE 4120 steel, the main steel material for sucker tools in oilfield production system, is usually subjected to the combined effects of stress and corrosive media in the oilfields corrosion environment containing CO₂. This work presented the evolution of pits and stress corrosion cracks in the steel while exposing to stress and corrosion medium. In the simulated oilfield environment, the four-point bending high temperature and high pressure stress corrosion test was carried out to investigate the evolution process of pits and stress corrosion cracks. The morphologies of pits and cracks were characterized by scanning electron microscopy to study the process of crack initiation and growth. In addition, the stress and strain distribution of corrosion pits was described using ABAQUS finite element analysis software to qualitatively analyze the vulnerable location of crack origin. The results exhibited that corrosion pits originated from inclusions, while the SCC initiated from the bottom of secondary corrosion pits and extended along the depth direction of SAE 4120 steel in the simulated oilfield environment with in water saturated with CO₂. Finite Element Analysis showed that the maximum values of stress and strain were located at corrosion pits bottom. The existing secondary corrosion increased the degree of stress concentration, and the bottom of the secondary corrosion pits was the sensitive position of SCC.

Keywords: SAE 4120 steel; Four-point bending test; Pitting corrosion; Stress corrosion crack; Finite element analysis

1. INTRODUCTION

SAE 4120 steel is the main steel material of sucker rod in oilfield production system. With the increase of water content and corrosive media such as CO₂ and Cl⁻ in the oil wells, the used steels are increasingly confronted with some problems, including local corrosion and stress corrosion damage [1-7]. Production and transportation pipelines and equipment used in oil and gas fields can easily fail under harsh service conditions or due to material quality. H. Ding et al. showed that under cyclic loading, the

residual height of the sucker rod in the inner side of the weld forms a crack source because of stress concentration at first then the crack propagates along the heat affected zone[8]. Haijun Shen et al. showed that the curves of SAE 4120 Steel based on the 3D model are obtained, and then the fatigue crack propagation life of the elliptical surface cracks in SAE 4120 Steel bars is predicted[9]. SCC originates from corrosion pits. The evolution of pitting will lead to the crack propagation, which results in the fracture failure of components. Meresht et al. showed that stress corrosion cracks of X60 pipeline steel originated from the bottom of the pit and extended along the thickness direction [10]. In addition, the element analysis for the crack tip showed that the crack started from the inclusions, The hydrogen-induced defect at the crack tip reduced the pH, thus the crack propagation was aggravated. Horner et al. displayed that 7% of cracks nucleated at the pit bottom, 50% originated from the shoulder of the pit. The others broke the pit shoulder and extended beyond the pit bottom. 3-D X-ray micro tomographic images also confirmed that most of cracks developed at the pit shoulder of cylindrical specimens and the stress could reach 50-90% of the yield strength [11]. Ryuichiro et al. considered that the cracks initiated from the pit bottom due to the presence of the maximum stress concentration and the active electrochemical potential [12]. Li et al. investigated the behavior of pit-stress corrosion cracks of 304 stainless steel with constant load [13]. It was emphasized that the SCC started from the sensitive point at the bottom and gradually extended to be stress corrosion fracture. The location of pitting is still controversial because of the crack initiation. Therefore, studying the pitting evolution and crack initiation location of SCC of SAE 4120 steel is significant to prolong the service life of components.

This work aims to investigate the pit position where the SCC crack is generated under high temperature and high pressure in simulated oil field environment. To begin with, the morphologies of cracks and pits were obtained by means of scanning electron microscopy to analyze the relationships between the SCC cracks and pits, as well as the characteristics of pit initiation and growth. In addition, an FE method was employed to examine the distribution of the stress and strain on pits and SCC cracks. Moreover, the mechanic and electrochemistry theories were applied to discuss the mechanisms of the initiation and growth of pitting, the early-stage SCC nucleation under load and the pit position where the crack most likely to occur.

2. EXPERIMENTS AND SIMULATION

2.1. SCC and pitting tests

SAE 4120 steel was used as the sample and the chemical composition was listed in Table 1.

Table 1. the chemical composition of SAE 4120 steel (wt.%)

chemical composition	C	Cr	Mo	Si	Ni	Mn	V	S	Fe
SAE 4120 steel	0.20	1.90	0.20	0.25	0.25	0.55	0.05	0.025	balance

All specimens were machined into rectangle coupons with a dimension of 116 mm ×16 mm×2 mm. The specimens were firstly polished successively with 200, 400, 600, 800 and 1500 grit sandpaper, cleaned with alcohol and acetone and then dried immediately.

After the pretreatment, the test vessel was filled with 2500 mL test solution to ensure that the samples were completely immersed. The composition of the test solution is given in Table 2. The simulated solution was poured into the autoclave and N₂ gas was injected for 4 h before introducing CO₂ to remove oxygen. The constant strain four-point bending test in ASTM G39 standard was adopted. The high temperature and high pressure test was carried out in 3 L high temperature and high pressure FCZ magnetic drive reactor. The schematic of a four-point bending fixture is shown in Fig. 1. The deflection calculation of four-point bending sample was obtained via the formula:

$$y = \frac{\sigma(3H^2 - 4A^2)}{12Et} \quad (1)$$

where σ is the maximum tensional stress (616 MPa), E is the elasticity modulus (253000 MPa), t is the thickness of the sample (2 mm); H is the distance between the pivot points (110 mm); A is the distance between the inner and outer fulcrum (27.5 mm); y is the maximum deflection. Therefore, the calculated deflection was 3.378 mm. According to the ASTM G39 standard, the value of applied stress was 90% yield strength. The conditions of field environmental were simulated at a CO₂ partial pressure of 3 MPa and temperature of 80 °C. The test duration were 1080 h, 2160 h, and 3240 h, respectively, which was determined by ASTM G31-2004.

After the tests, each sample was ultrasonically cleaned with alcohol and acetone, and then dried immediately. Subsequently, the morphologies of SCC cracks and pits on the side perpendicular to the thickness direction were observed by means of SEM. Each sample was characterized by X-ray diffractometry (XRD) for bulk phase identification, and scanning electron microscopy/energy dispersive X-ray spectrometry (SEM/EDS) for microstructure and phase constituents. The samples were characterized using XRD to identify the phase constituents. The X-ray diffraction test was conducted with Nova Nano SEM450 X-ray diffractometer under these conditions: Cu-K α X-ray source; High vacuum mode resolution: 1nm (15kV), 1.6 nm (1kV); Low vacuum mode resolution: 1.5nm (10kV, Helix detector), 1.8nm (3kV, Helix detector); scanning range of $2\theta = -10-70^\circ$; Magnification of standard sample: 40 times ~ 400,000 times. Detection and mapping of elements in samples with the Oxford X-Max 80 energy dispersive spectrometer (EDS) equipped. The EDS energy spectrum energy resolution was 126eV, composition range of B ~ U, about 1 m beam spot affected area.

Table 2. Composition of oilfield produced fluid

Ingredient	K ⁺	Na ⁺	Ca ²⁺	Cl ⁻	SO ₄ ²⁻	Mg ²⁺	HCO ₃ ⁻
Content (mg/L)	3.13	5912.47	134.67	8862.50	69.16	140.03	1463.82

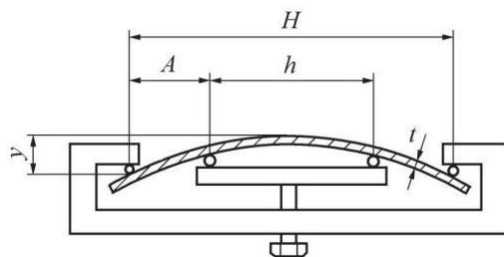


Figure 1. The size of four point bending specimen

2.2. Finite element analysis

FE analysis was carried out using ABAQUS. A 3-D version of the specimen was modelled in the ABAQUS CAE pre-processor. The mesh was created using 3-D elements C3D4, which are 4-node linear tetrahedral elements, and was refined in the region around the pit to enhance the prediction accuracy of stress and strain. The four-point bending finite element model of assembly drawing is shown in Fig. 2. As exhibited in Fig. 3, a pit was created at half the length of the specimen. The diameter and depth of the primary corrosion pit were 120 μm and 40 μm , respectively, and the corresponding dimensions of the secondary corrosion pit were 10 μm and 5 μm . Boundary conditions were applied to the ends of the specimen to ensure the specimen alignment during loading.

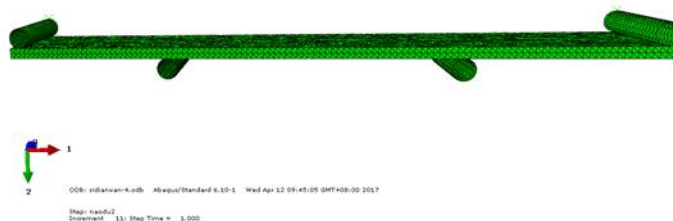


Figure 2. Four-point bending finite element model of assembly drawing

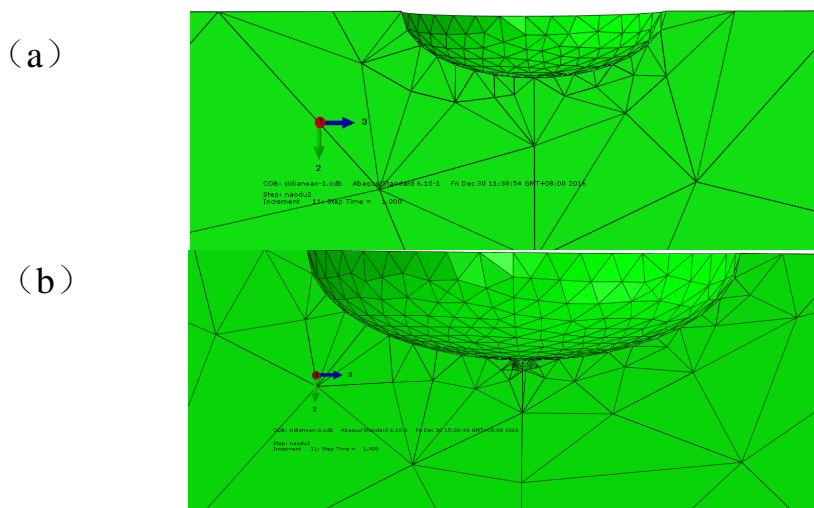


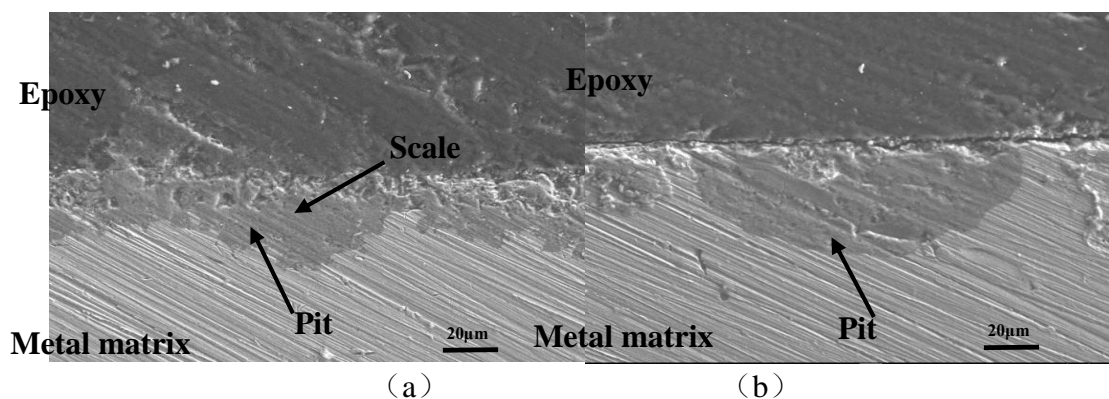
Figure 3. Specimen geometry of pit used for finite element analysis. (a) pit without secondary pit; (b) pit with secondary pit.

The boundary conditions were as follows: $U1=U2=U3=UR1=UR2=UR3=0$. To take account for the test displacement load, a displacement load of -3.378 mm was applied in the “2” direction, which was consistent with the deflection values in stress corrosion test. In this paper, degree of freedom U1: translational degree of freedom along the X-axis; U2: translational degrees of freedom along the y-direction of the coordinate axis; Degree of freedom U3: translational degree of freedom along the direction of coordinate axis Z; Degree of freedom UR1: the degree of rotation along the x-direction of the coordinate axis; Degree of freedom UR2: translational degree of rotation along the y-direction of coordinate axis; Degrees of freedom UR3: translational degrees of rotation along the Z axis. The input parameters for the EF model include Young modulus of 210 GPa, yield strength of 685 MPa and Poisson's ratio of 0.3 for the SAE 4120 steel. The stress, S11, and the strain, LE11, in the “1” direction were used in the analysis to characterize the elastic behavior of the material.

3. RESULTS AND DISCUSSION

3.1 High temperature and high pressure constant strain four point bending test

A wire cutting was made at the location of the pit to obtain the cut surface. Inserted the specimen into an epoxy resin and polished it. The morphologies of different cross-sections perpendicular to the sample thickness direction are shown in Fig. 4. The pits and cracks can easily be detected by SEM. The nucleation and growth process of corrosion pits can be noted in Fig. 4(a) and (b). The transition from corrosion pit to crack are displayed in Fig. 5(a). It is found that the crack originated from the bottom of the pit and extended along the depth direction of specimen. In addition, secondary corrosion pits formed at the bottom of the corrosion pit hence the increase of stress concentration. According to Ref.[14], once a secondary pit nucleated at the bottom of the primary pit, the stress distribution would change entirely and the overall value of stress concentration factor (SCF) would be much higher than the single primary pit [14-15]. Accordingly the existence of secondary corrosion pits increases the occurrence tendency of SCC.



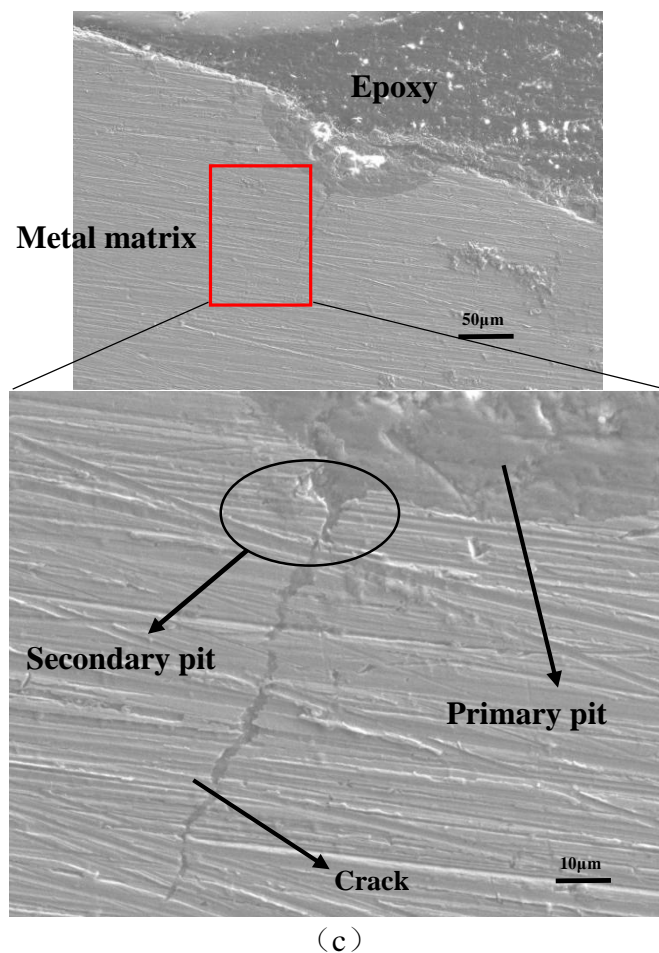


Figure 4. The SEM of cross section of SAE 4120 steel after four-point bending stress corrosion experiment

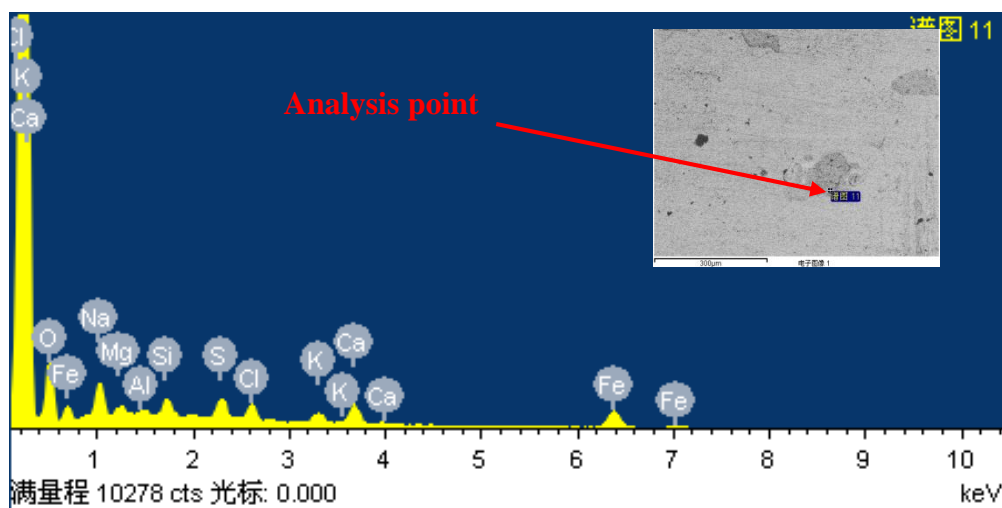


Figure 5. EDS spectra for of corrosion pit

Table 3. Element percentage of corrosion pit

Element	O	Na	Mg	Al	Si	S	Cl	K	Ca	Fe
Percentage (%)	54.67	11.54	1.99	0.86	3.15	4.55	3.97	2.54	5.19	11.54

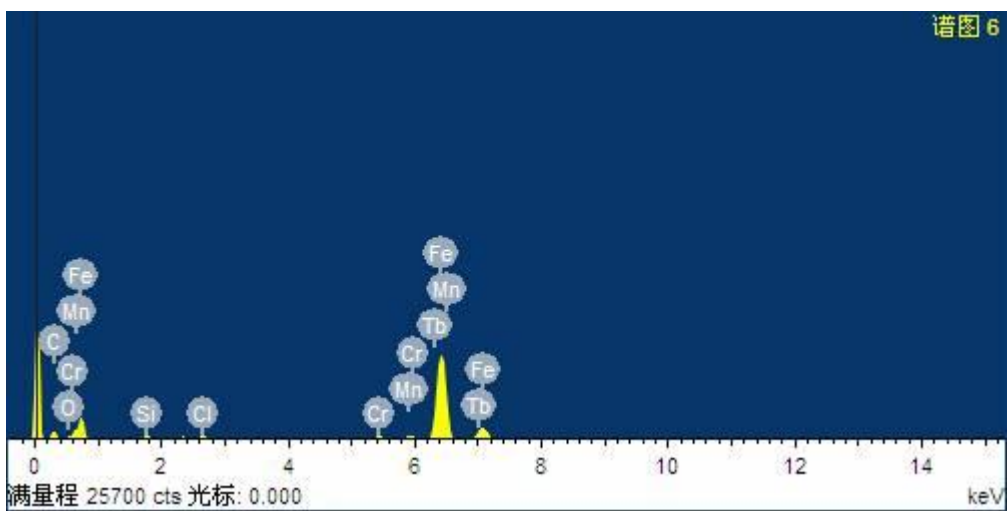


Figure 6. EDS spectrum for uncorroded area.

Table 4. Element percentage of uncorroded area

Element	C	O	Si	Cl	Cr	Mn	Fe	Tb
Percentage (%)	25.15	1.66	0.39	0.24	0.61	1.01	69.11	1.84

The EDS spectrum displayed in Fig. 5 and Fig. 6 reveals more Mg and Al in the corrosion pits than uncorroded area. The pit firstly nucleated at the inclusion, and the corrosion pit formed around the center of the inclusion. The Fe as the anode on the boundary between the inclusion and the steel matrix dissolved firstly, and the inclusions acted as the cathode[16]. With the extension of corrosion time, corrosion pits appeared. The corrosion medium entered the corrosion pits and continued to corrode the steel matrix. As the reaction progressed, the pH value decreased gradually, which accelerated the dissolution rate of the steel. The decreased pH value could be attributed to the hydrolysis of some metal cations. In addition, the other metal cations diffused into the area around the corrosion pit and hydrolysis reactions increasingly enlarged the pitting area [17]. The pH value of the cathode region far from the inclusions was higher than that of the corrosion pit, causing the diffused metal cations to become precipitates, such as hydroxides or oxides [18]. When the inclusions were completely dissolved, the chloride ions diffused into the pits and continued to erode the metal matrix, hence the corrosion pits continued to expand in the depth direction of the steel matrix.

3.2 Finite element simulation results

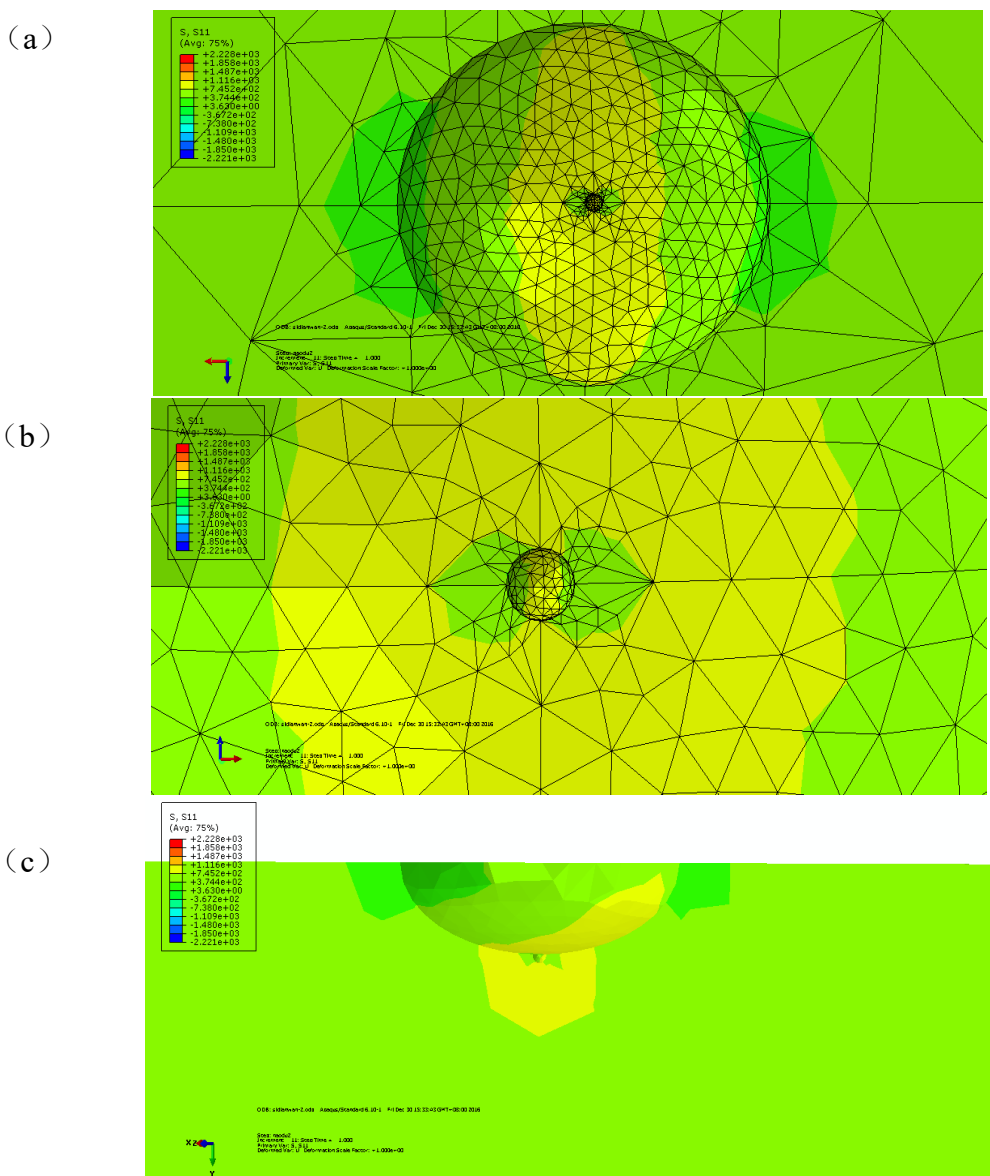
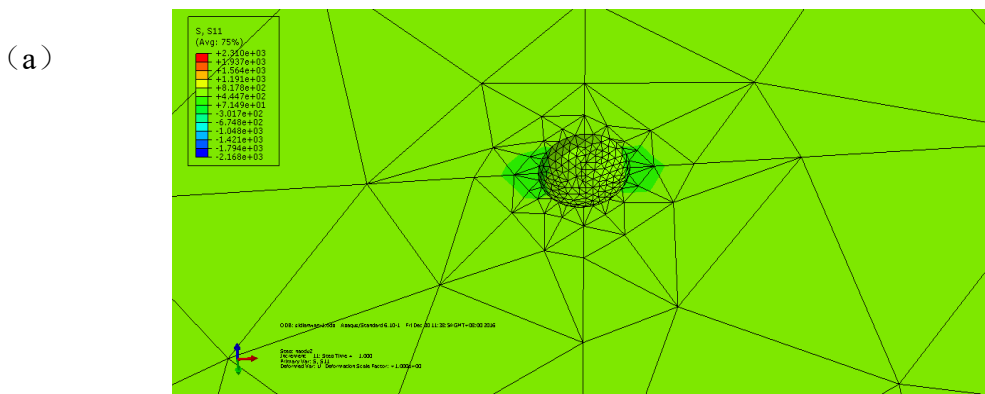


Figure 7. Stress distribution with secondary corrosion pit (a) Global local stress distribution plan view; (b) Local stress distribution plan view; (c) Stress distribution cross-section view.



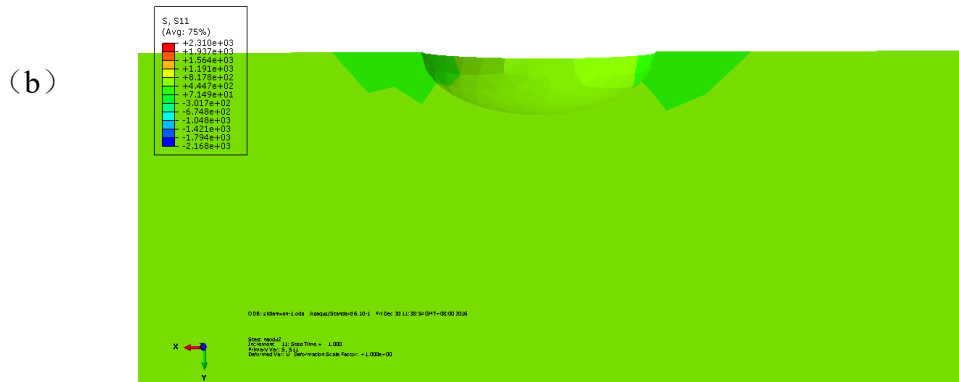


Figure 8. Stress distribution view without secondary corrosion pit (a) Stress distribution plan view; (b) Stress distribution cross-section view

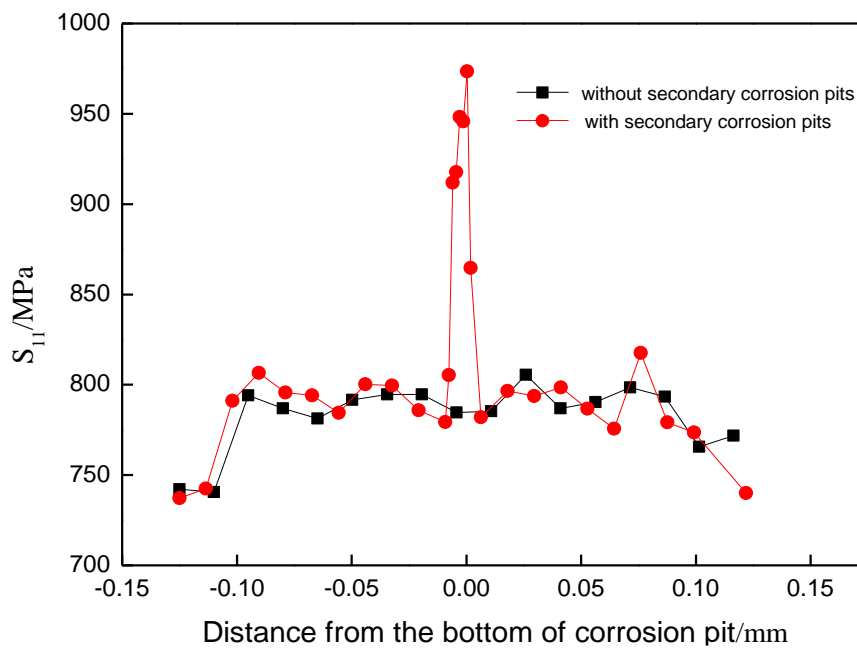
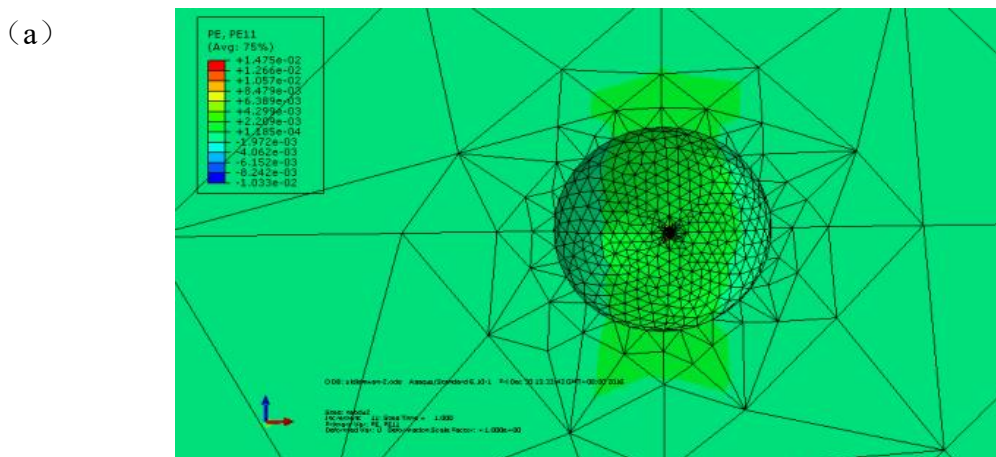


Figure 9. Stress distribution curve of the corrosion pit half elliptical path along the width direction of four-point bending specimen



(b)

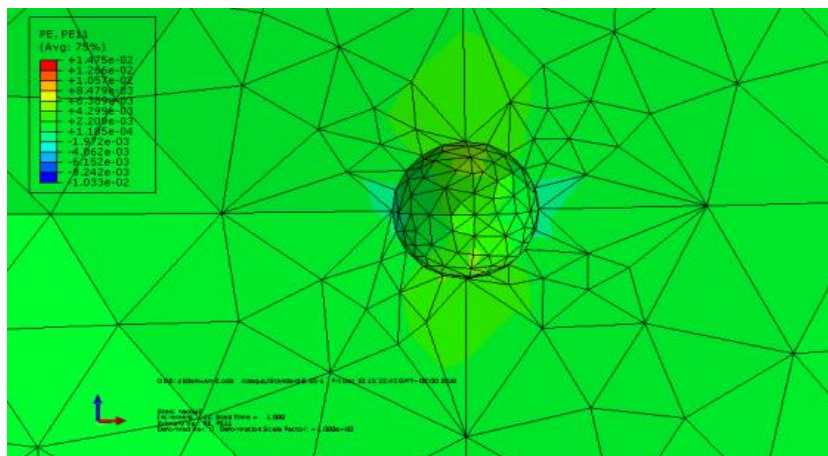


Figure 10. Strain distribution with secondary pit (a)Global strain distribution plan view; (b) Strain distribution drawing of partial enlargement

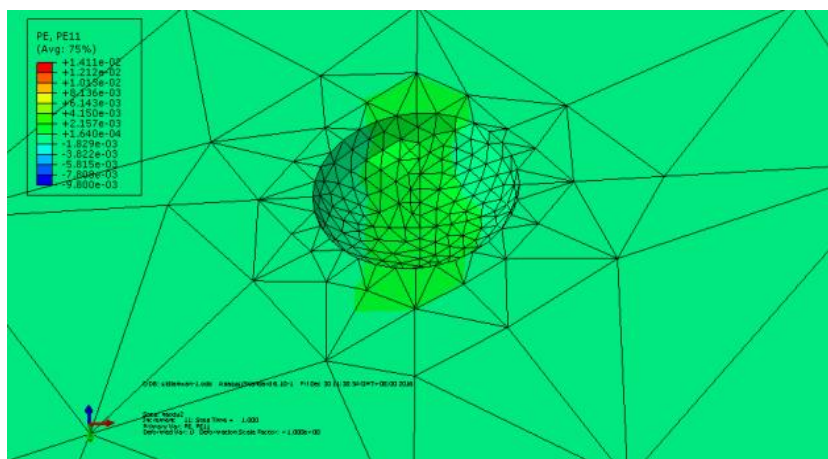


Figure 11. Strain distribution without secondary corrosion pit

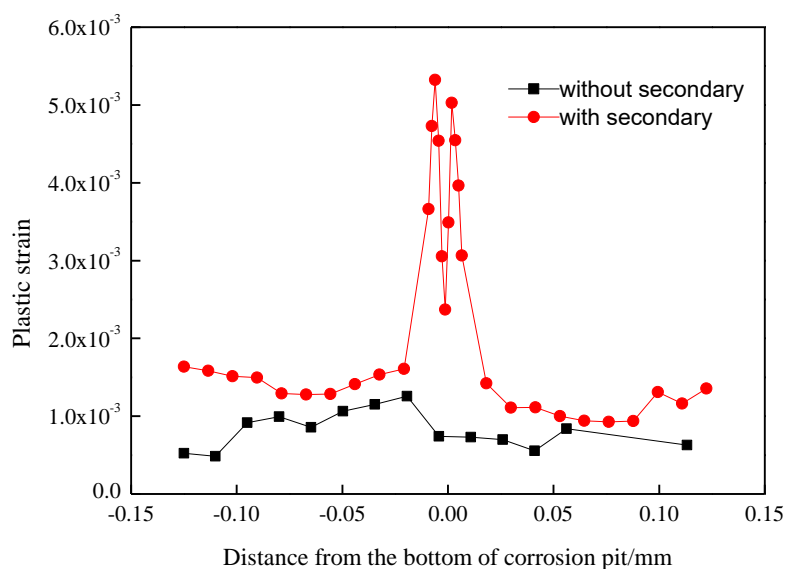


Figure 12. Strain distribution curve of the corrosion pit half elliptical path along the width direction of four-point bending specimen

An FE method was used to evaluate the normal stresses, S11, and the normal strains, LE11, distributed on specimens with and without secondary corrosion pits. As seen in Fig. 7 and Fig. 8, the region of maximum stress between the two lower supports of four-point bending specimen appeared near the bottom of the corrosion pit. Based on Fig. 9, the maximum value of normal stress with secondary corrosion pits was 973.5 MPa, while the maximum stress value was 805.5 MPa without secondary corrosion pits. It can be seen that the material had been subjected to an excessive yield strength and the plastic strain had occurred. The conclusion in line with Alan Turnbull’s viewpoint[19]. While at very high applied stress where plastic deformation occurs, the crack originated at the pit base. In addition, according to the Fig. 9, it can be found that the stress concentration factor increased with the occurrence of secondary corrosion pits. From Fig. 10, the maximum value of normal strain was 5.32×10^{-3} , locating at the mouth of the secondary corrosion pit. The maximum value of normal strain with secondary pit was four times larger than that without secondary pit at the bottom.

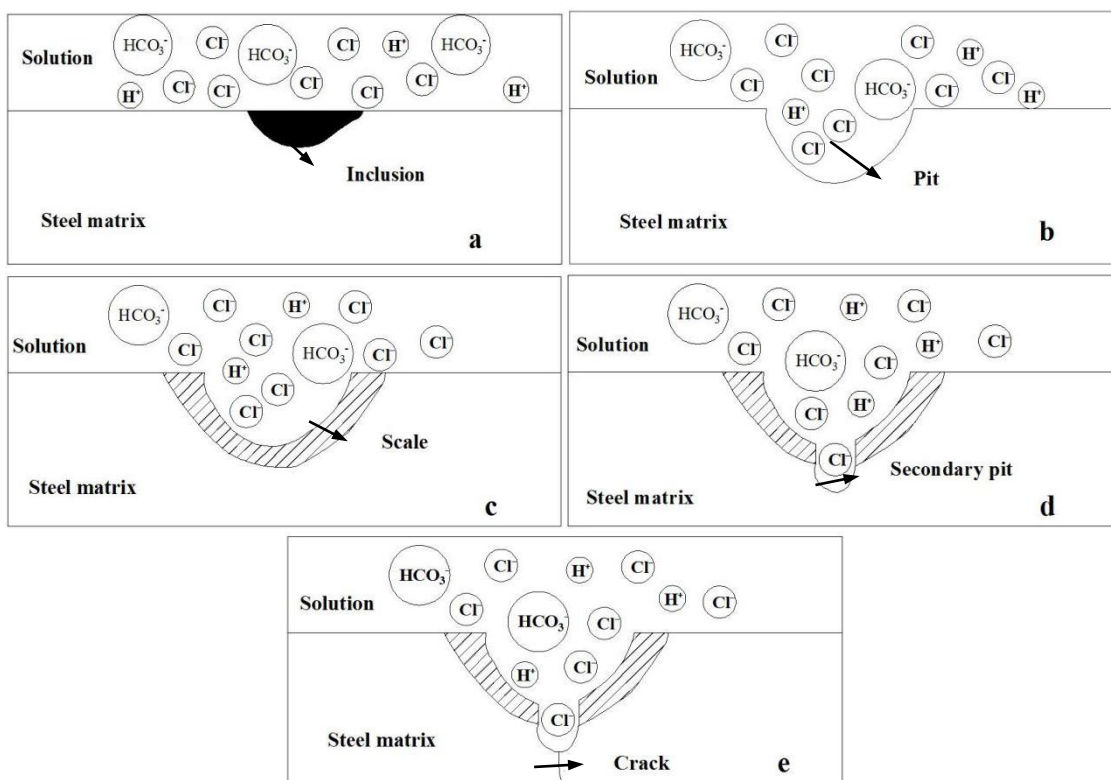


Figure 12. Pitting corrosion evolution mechanism model

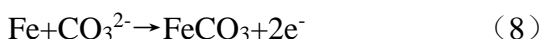
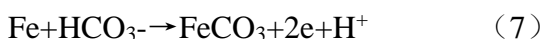
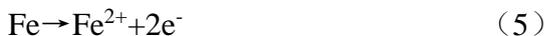
The mechanism of pitting evolution consists of five parts, as shown in Fig. 13. Pit initiation and growth are an essentially electrochemical process. For pit initiation, the stochastic and deterministic models have been proposed during the past decades. Experimental results showed that the pits nucleated near inclusions, and a corrosion cell was formed in the region around inclusions, as shown in Fig. 13(a). With the increase of corrosion time, the corrosion pits appeared. The corrosion medium entered the corrosion pits and the pH values in the pits decreased with the reaction. As a result, the dissolution rate of the steel matrix accelerated and the pitting pits began to grow (Fig. 13(b)). In Fig. 13(c), due to the

presence of corrosive medium, such as Cl^- , CO_2 and other corrosive medium, the reaction process is as follows[20]:

Cathodic reaction:



Anodic reaction:



Therefore, the anodic reactions of SAE 4120 steel in the CO_2 -saturated water include reactions (5) and (6), i.e., the direct dissolution of Fe via $\text{Fe} \rightarrow \text{Fe}^{2+} + 2\text{e}^-$ and the formation of corrosion scale FeCO_3 via $\text{Fe} + \text{HCO}_3^- \rightarrow \text{FeCO}_3 + 2\text{e}^- + \text{H}^+$. When the dense corrosion product FeCO_3 is formed, it will cover the corrosion pits, which isolates the corrosive ions and protects the metal matrix. However, the tensile stress will result in the formation of a gap on the corrosion product film. At the same time, due to the presence of Cl^- corrosion medium with high concentration and small diameter, corrosion products and Cl^- will penetrate into the interface between metal matrix and corrosion product film. Besides, The concentration of Cl^- at the interface increases because the structure of the electric double layer is subject to the preferential adsorption of Cl^- [21]. The Cl^- is accumulated constantly in the pitting pits and accelerates the pit growth. The Cl^- quickens the dissolution of iron matrix owing to the autocatalytic mechanism, the reaction is given as [22]:



The Cl^- is preferentially absorbed by the metal surface while coexisting with other ions [23]. A large amount of Cl^- can polymerize between the metal surface and corrosion product film, resulting in the reduction of adhesion of the corrosion product film. The corrosion products of the metal fall off the metal substrate easily. Therefore, the increase of Cl^- content results in the increase of cracks and reduces the bonding strength between the corrosion products and the metal matrix [24]. As the autocatalytic reaction continues at the bottom of the pit, from Fig. 12(b), the secondary corrosion pits will appear at the bottom of the pit, leading to a greater concentration of stress and greater plasticity. The stress potential (E11) and the strain potential (V11) are proportional to the stress (S11) and the strain (LE11), respectively [25]:

$$E112 \propto S112 \quad (12)$$

$$V112 \propto LE112 \quad (13)$$

The FE results revealed that the maximum stress and strain with secondary corrosion pits were higher than those without secondary corrosion pits. Local stress or strain provided favorable conditions for the formation of negative potential on the surface. According to the formula (12) and (13), the maximum stress and strain values with secondary corrosion pits are respectively 1.28 times and 4 times larger than those without secondary corrosion pits, resulting in a higher stress potential and strain potential. This is conducive to the production of anodic dissolution and the increase of corrosion rate. The growth rate of corrosion pits along the thickness direction is faster than other directions during the

expansion process due to the existence of the corrosive medium and the larger stress and strain at the bottom of the corrosion pit [26]. When the corrosion pit depth reaches the critical value, the pit will transform into the SCC [27].

4. CONCLUSION

(1) In the simulated oilfield environment with CO₂-saturated water, the pitting corrosion originates from inclusions, while SCC originates from the secondary corrosion pits at the bottom of pits and extends along the depth direction of SAE 4120 steel.

(2) FE analysis demonstrates that the maximum values of stress and strain are located at the bottom of corrosion pits. The existence of secondary corrosion increases the degree of stress concentration, and the bottom of secondary corrosion pits is the sensitive position of SCC.

ACKNOWLEDGMENTS

The authors gratefully acknowledge the support from Fundamental Research Funds for the Central Universities (18CX05002A) and the Natural Science Foundation of Shandong Province (ZR2019MEE108).

References

1. Y.M. Zeng, K.Y. Li, *Corros. Sci.*, 165(2020)108404.
2. J.W. Yang, L. Zhang, R.M. Ding, J.B. Sun and M.X. Lu, *Acta Metall.Sinica.*, 44(2008)1366.
3. K. Majchrowicz, T. Brynk, M. Wiczorek, D. Miedzinska and Z. Pakiela, *Eng. Fail. Anal.*, 104(2019):471.
4. K. Ravindranath, B.A. Wakaa, N. Tanoli, *Eng. Fail. Anal.*, 74(2017):142.
5. S.D. Zhu, J.F. Wei, Z.Q. Bai, G.S. Zhou, J. Miao and R.Cai, *Eng. Fail. Anal.*, 18(2011):950.
6. E.E.A.E. Aal, S.A.E. Wanees, A. Diab, E. Haleem and S.M.A.E. Haleem, *Corros. Sci.*, 51(2009)1611.
7. A. Rajabipour, R.E. Melchers, *Int. J. Hydrogen Energy*, 40(2015)9388.
8. H. Ding, A.B. Zhang, D.T. Qi, H.B. Li, P.L. Ge, G.Q. Qi, N. Ding, Z.Q. Bai and L. Fan, *Eng. Fail. Anal.*, 109(2020)104300.
9. H.J. Shen, W.L. Guo, *Int. J. Fatigue*, 27 (2005) 617.
10. E.S. Meresht, T.S. Farahani, J. Neshati, *Eng. Fail. Anal.*, 18(2011)963.
11. D.A. Horner, B.J. Connolly, S. Zhou, L. Crocker and A. Turnbull, *Corros. Sci.*, 53(2011)3466.
12. R. Ebara, *Mater. Sci. Eng. A*, 468-470(2007)109.
13. D.T. Spencer, M.R. Edwards, M.R. Wenman, C. Tsitsios, G.G. Scatigno, P.R. Chard-Tuckey and M.R. Wenman, *Corros. Sci.*, 88(2014)76.
14. M. Cerit, K. Genel, S. Eksi, *Eng. Fail. Anal.*, 16(2009)2467.
15. I.F.Z. Tello, G.M.D. Almaraz, V.L. Garza and M.G. Tapia, *Adv. Eng. Software*, 131(2019)23.
16. J. Villavicencio, N. Ulloa, L. Lozada, M. Moreno and L. Castro, *J. Mater. Res. Technol.*, 9(2020)5894.
17. Y. Tsutsumi, A. Nishikata, T. Tsuru, *Corros. Sci.*, 49(2007)1394.
18. T.G. Duan, W.S. Peng, K.K. Ding, W.M. Guo, J. Hou, W.H. Cheng, S.T. Liu and L.K. Xu, *Ocean Eng.*, 189(2019)106405.
19. A. Turnbull, L. Wright, L. Crocker, *Corros. Sci.*, 52 (2010) 1492.
20. L. Pang, Z.B. Wang, Y.G. Zheng, X.M. Lai, X. Han, *J. Mater. Sci. Technol.*, 54(2020)95.
21. C.D. Taylor, S.R. Li, A.J. Samin, *Electrochim. Acta*, 269(2018)93.

22. D.Hecht, P. Borthen, H.H. Strehblow, *Surf. Sci.*, 365(1996)263.
23. T.P. Hoar, D.C. Mears, G.P. Rothwell, *Corros. Sci.*, 5(1965)279.
24. Q.Y. Liu, L.J. Mao, S.W. Zhou, *Corros. Sci.*, 84(2014)165.
25. J. Weertman, *Mech. Mater.*, 37(2005)543.
26. N. Aouina, F. Balbaud-Célérier, F. Huet, *Electrochim. Acta*, 104(2013)274.
27. Z.Z. Guo, Y.F. Ma, L. Wang and J.R. Zhang, *Eng. Fail. Anal.*, 105(2019)883.

© 2021 The Authors. Published by ESG (www.electrochemsci.org). This article is an open access article distributed under the terms and conditions of the Creative Commons Attribution license (<http://creativecommons.org/licenses/by/4.0/>).